

This work was written as part of one of the author's official duties as an Employee of the United States Government and is therefore a work of the United States Government. In accordance with 17 U.S.C. 105, no copyright protection is available for such works under U.S. Law. Access to this work was provided by the University of Maryland, Baltimore County (UMBC) ScholarWorks@UMBC digital repository on the Maryland Shared Open Access (MD-SOAR) platform.

Please provide feedback

Please support the ScholarWorks@UMBC repository by emailing [scholarworks-group@umbc.edu](mailto:scholarworks-group@umbc.edu) and telling us what having access to this work means to you and why it's important to you. Thank you.

# Influence of losses on the superresolution performances of an impedance-matched negative-index material

Giuseppe D'Aguanno,\* Nadia Mattiucci, and Mark J. Bloemer

Charles M. Bowden Research Center, Research, Development, and Engineering Command, Building 7804,  
Redstone Arsenal, Alabama 35898-5000, USA

\*Corresponding author: giuseppe.daguanno@us.army.mil

Received September 6, 2007; revised November 21, 2007; accepted November 25, 2007;  
posted December 6, 2007 (Doc. ID 87270); published January 29, 2008

We discuss by a Poynting vector analysis how the losses of a negative-index material (NIM) affect the resolution performances of a Veselago–Pendry lens, and we analyze those performances in the framework of the Abbe criterion. The limits of both high losses and low losses are explored. We find that the impedance-matched NIM is able to resolve 30% better than the limit imposed by the Abbe criterion even when the imaginary part of the refractive index (the material losses) exceeds the absolute value of the real part of the refractive index. The NIM is described by a lossy Drude model with equal permittivity and permeability. By increasing the damping parameter of the Drude model, we also explore the regime where both permittivity and permeability are positive and point out the conditions under which the metamaterial is still able to superresolve. © 2008 Optical Society of America

OCIS codes: 160.3918, 260.1960, 180.4243.

## 1. INTRODUCTION

In the past few years, negative-index materials (NIMs), i.e., materials that have simultaneously negative permittivity and magnetic permeability [1], have been the subject of intense theoretical and experimental investigations [2–5]. Several applications have been envisioned for those materials [6–9], although, arguably, the most important is the possibility to use them to construct a “perfect” lens, i.e., a lens that can also focus the evanescent near-field components of an object, as pointed out by Pendry several years ago in his seminal paper [2]. One serious issue that plays a detrimental role toward the achievement of a superresolving lens is the fact that in currently available metamaterials the absorption is still very high. To characterize the quality of a NIM it is helpful to introduce its figure of merit (FOM), defined as  $\text{FOM} = -\text{Re}(\hat{n})/\text{Im}(\hat{n})$ , where  $\hat{n}$  is the complex refractive index of the NIM. The path toward the realization of NIMs in the near-infrared and visible regimes with high FOMs is still long, although remarkable progress has been made very recently. In 2005 the first NIMs operating in the visible regime were reported [10,11], and shortly thereafter a low-loss silver-based NIM operating at telecommunication wavelengths was theoretically studied [12] and experimentally realized [13] with a FOM  $\sim 3$  at  $\sim 1.5 \mu\text{m}$ . Recently, negative-index metamaterials operating at 780 nm with a FOM  $\sim 0.5$  [14] and at 813 nm with a FOM  $\sim 1$  [15] have been realized and tested.

The aim of this work is twofold: first, to study how the losses and the FOM of the NIM influence its capability to act as a superresolving lens, and second, to assess what is in principle the maximum resolution power achievable in a NIM-based lens. As a prototype and benchmark of a

NIM-based device for superresolution purposes, we study the configuration described in Fig. 1. In Fig. 1 the distance between the object plane and the input surface of the lens  $d_1$  and the distance of the image plane from the output surface of the lens  $d_2$  are chosen according to the geometrical rule  $d_2 = L - d_1$ , where  $L$  is the thickness of the NIM slab. This is the geometrical rule that assures the optimum image formation for a flat lens with refractive index  $n = -1$ , as pointed out in [2].

To avoid any ambiguity we have chosen to study two pointlike sources; i.e., we consider two slits in the object plane whose dimension is  $\sim 1/500$ th of the incident wavelength  $\lambda$  so that, for all intents and purposes, the limit of point source is reached. The mutual distance  $D$  between the two points is therefore the only parameter that characterizes the source. The calculations of the diffraction figures on the image plane have been carried out using the technique of the angular spectrum decomposition in conjunction with the transfer matrix technique [16]. More details about the calculation technique can be found in Appendix A. The permittivity and permeability of the NIM are described with a degenerate, lossy Drude model [2]:  $\hat{\epsilon}(\tilde{\omega}) = \hat{\mu}(\tilde{\omega}) = \hat{n}(\tilde{\omega}) = 1 - 1/[\tilde{\omega}(\tilde{\omega} + i\tilde{\gamma})]$ , where  $\tilde{\omega} = \omega/\omega_{ep}$  is the normalized frequency,  $\omega_{ep} = 2\pi c/\lambda_{ep}$  is the electric plasma frequency,  $\lambda_{ep}$  is the corresponding wavelength, and  $\tilde{\gamma} = \gamma/\omega_{ep}$  is the damping term normalized with respect to the electric plasma frequency. Note that here we are supposing that the electric and magnetic plasma frequency are equal, i.e.,  $\omega_{ep} = \omega_{em}$ . The condition  $\hat{\epsilon} = \hat{\mu} = \hat{n}$  obviously implies that the impedance of the medium  $Z = \sqrt{\hat{\mu}/\hat{\epsilon}}$  is perfectly matched with the impedance of vacuum ( $Z = 1$ ) for any value of the damping term and any value of the refractive index. Note also that, while we are

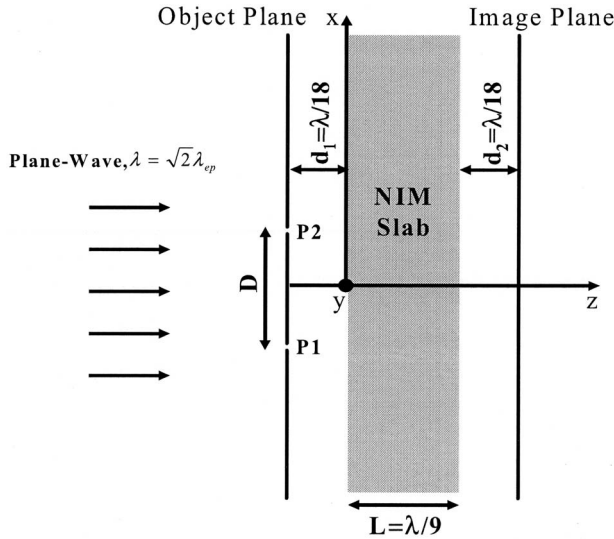


Fig. 1. A plane, monochromatic wave at the operative wavelength  $\lambda$  is incident on a screen of negligible thickness with two very small apertures or slits (P1 and P2) that act as pointlike sources (dimension of  $\sim 1/500$ th of the incident wavelength) whose mutual distance is  $D$ . A slab of NIM  $L = \lambda/9$  in length, placed at a distance  $d_1 = \lambda/18$  from the object plane, captures the light diffracted from the two slits and focuses it on the image plane placed at a distance  $d_2 = \lambda/18$  from the end of the NIM slab. The image plane is chosen following the geometrical rule for the image formation:  $d_2 = L - d_1$ .

always in a condition of impedance matched, the particular condition  $n = -1$  has the further advantage with respect to the simple condition of impedance matched to reduce the reflection for a wider range of incident angles. Among metamaterials with superresolution capabilities, impedance-matched metamaterials play an important role, because their response is independent from the particular polarization of the incident light and therefore the superresolving capabilities are the same both for TE and TM light polarization. For instance, in [17] Aydin *et al.* report an impedance-matched, low-loss negative-index metamaterial superlens operating in the microwave regime (3.74 GHz) that is capable of resolving subwavelength features of a point source with a  $0.13\lambda$  resolution.

We fix the operative wavelength at  $\lambda = \sqrt{2}\lambda_{ep}$  so that the real part of the refractive index of the NIM is approximately  $-1$  for low values of the damping term. For example, at  $\lambda \sim 360$  nm the length of the NIM slab and the distances between the object plane and the image plane are the same as those reported in [2] for the superresolving lens described by Pendry. At the operative wavelength  $\lambda = \sqrt{2}\lambda_{ep}$  the expression of the refractive index and of the FOM are the following:

$$\text{Re}(\hat{n}) = \frac{-1 + 2\tilde{\gamma}^2}{1 + 2\tilde{\gamma}^2}, \quad \text{Im}(\hat{n}) = \frac{2\sqrt{2}\tilde{\gamma}}{1 + 2\tilde{\gamma}^2}, \quad \text{FOM} = \frac{1 - 2\tilde{\gamma}^2}{2\sqrt{2}\tilde{\gamma}}.$$

In Fig. 2 we show the FOM of the NIM and its refractive index at the operative wavelength  $\lambda = \sqrt{2}\lambda_{ep}$  as function of

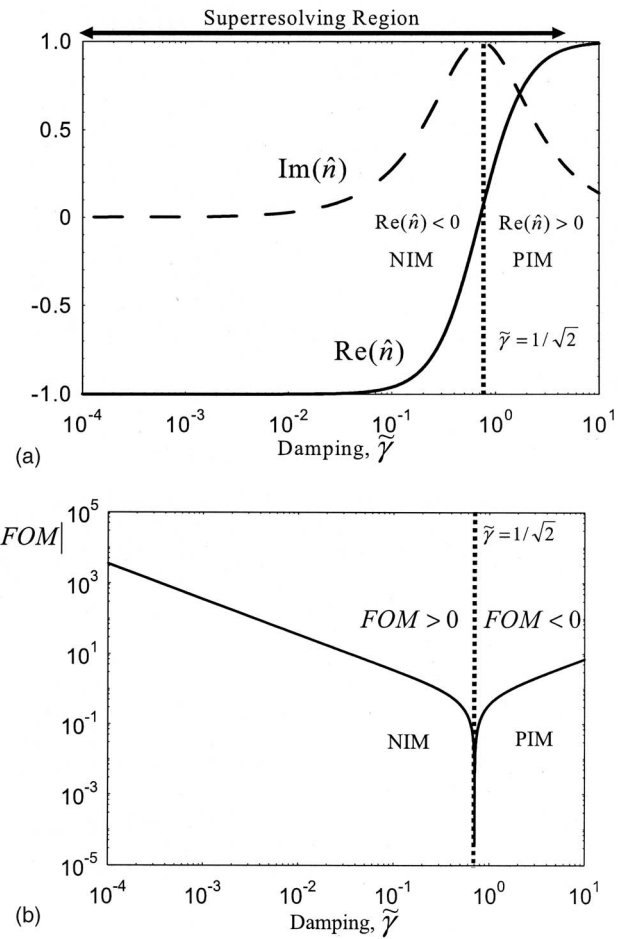


Fig. 2. (a) Real (solid curve) and imaginary part (dashed curve) of the refractive index versus the damping term ( $\tilde{\gamma}$ ) for a wavelength  $\lambda = \sqrt{2}\lambda_{ep}$ . The horizontal line with double arrows indicates the region where the metamaterial superresolves, i.e., when it resolves two point sources whose mutual distance is less than  $0.6\lambda$  with a visibility  $V \sim 50\%$ . The superresolving region extends from  $\tilde{\gamma} = 0^+$  to  $\tilde{\gamma} \approx 3.5$ , which correspond respectively to a refractive index of  $\hat{n} = -1 + i0^+$  and  $\hat{n} \approx 0.92 + i0.38$ . (b) Figure of merit (FOM) versus the damping term ( $\tilde{\gamma}$ ). In both figures the vertical line indicates the position of  $\tilde{\gamma} = 1/\sqrt{2}$ , which corresponds to the transition of the metamaterial from a true NIM to a positive-index material (PIM).

the damping term  $\tilde{\gamma}$ . The figures clearly identify two regimes: 1) for  $\tilde{\gamma} < 1/\sqrt{2}$  we have that  $\text{Re}(\hat{n}) < 0$  and  $\text{FOM} > 0$ , i.e., the metamaterial acts as a true NIM; 2) for  $\tilde{\gamma} > 1/\sqrt{2}$  we have that  $\text{Re}(\hat{n}) > 0$  and  $\text{FOM} < 0$ , i.e., the metamaterial acts as a positive-index material (PIM). For  $\tilde{\gamma} = 1/\sqrt{2}$  the refractive index is a pure imaginary number,  $\hat{\epsilon} = \hat{\mu} = \hat{n} = i$ , and the metamaterial acts as an impedance matched material having the real part of the refractive index equal to zero. For the sake of clarity we have also reported in Fig. 2(a) the region where the metamaterial superresolves, which is one of the main results of our analysis. We will give the details below, suffice here to note that the metamaterial superresolves even in the region where it behaves as a PIM. Before going into the details of our analysis it is worthwhile to recall the classical limit under which two pointlike objects cannot be resolved; this limit is sometimes also known as the "Abbe

criterion" [18]. The Abbe criterion states that the smallest distance between two pointlike objects that an optical instrument, such as a classical microscope, can resolve is  $\sim 0.6\lambda/(n \sin \theta)$  where  $n$  is the refractive index of the immersion medium and  $\theta$  is the half-angle subtended by the object at the lens [18]. The two objects can be considered resolved when the image contrast or visibility ( $V$ ) of the diffraction figure is at least  $\sim 50\%$ , where  $V(\%) = 100(I_{\max} - I_{\min})/(I_{\max} + I_{\min})$  and  $I_{\max}$  and  $I_{\min}$  are, respectively, the maximum and minimum intensities of the diffraction figure. In principle the Abbe criterion does not prevent subwavelength resolution. In our case the immersion medium is air; therefore even assuming an infinitely extended lens so that  $\theta \sim \pi/2$  we obtain that the smallest distance is  $\sim 0.6\lambda$ . It is also worthwhile to spend few words regarding the properties of Pendry's perfect lens [2]. There are two equally important characteristics that contribute to make Pendry's lens "perfect." The first one is that the lens is flat and has a refraction index  $n = -1$ . Therefore, speaking in terms of geometrical optics, it focuses all the rays in only one point, avoiding the problem of spherical aberrations, which are typical of conventional curved lenses. The second characteristic is that the lens is able to reconstruct or amplify the near-field components of the object, giving, therefore, the possibility of beating the Abbe criterion. One of the findings of this work is that the possibility of beating the Abbe criterion can be achieved even when the lens is significantly off the ideal condition of  $n = -1$ , and therefore its focusing properties are less than ideal, because aberrations come into play. On the other hand, the condition of ideal focusing alone without the reconstruction or amplification of the evanes-

cent modes seems insufficient for beating the Abbe criterion. At this point an outstanding example of a flat lens in the form of a two-dimensional photonic crystal with an effective index  $n = -1$  and almost ideal focusing properties, but negligible reconstruction of the evanescent modes, can be found in [19]. In the work cited in [19] subwavelength resolution but not superresolution is achieved, i.e., the lens does not beat the Abbe criterion. Keeping in mind the above considerations, let us now analyze our results. The paper is organized as follows: In Section 2 we analyze the regime where  $\tilde{\gamma} < 1/\sqrt{2}$  and in Section 3 the regime where  $\tilde{\gamma} > 1/\sqrt{2}$ . In Section 4 we analyze the realistic case of a single layer of silver, and finally in Section 5 we go to the conclusions.

## 2. SUPERRESOLUTION FOR $\tilde{\gamma} \leq 1/\sqrt{2}$ (FOM $\geq 0$ )

As mentioned Section 1, in the case at hand the metamaterial acts as a true NIM with  $\text{Re}(\hat{n}) < 0$  and  $\text{FOM} > 0$ . First we analyze the case when the square modulus of the fields is considered, electric field for TE polarization or magnetic field for TM polarization. In Fig. 3 we show the diffraction figures and the minimum distance ( $D_{\min}$ ) that the NIM lens is able to resolve (according to a field analysis) for a FOM of  $\sim 3500$  [Fig. 3(a)],  $\sim 350$  [Fig. 3(b)],  $\sim 35$  [Fig. 3(c)], and  $\sim 3.5$  [Fig. 3(d)]. In Fig. 4 we show  $1/D_{\min}$  as function of the FOM for values of the FOM ranging from  $10^{-4}$  to  $10^4$ . The figure suggests that the scaling law of the minimum resolved distance as function of the FOM is as follows:

$$D_{\min} \cong \begin{cases} \frac{\lambda}{2 \log(\text{FOM})} \cong \frac{\lambda}{2 |\log(\text{Im}(\hat{n}))|} & \text{for FOM} \gg 1, \quad \text{Im}(\hat{n}) \ll 1 \\ 0.4\lambda & \text{for } 0 \leq \text{FOM} \leq 1, \quad \text{Im}(\hat{n}) \cong 1 \end{cases} \quad (1)$$

The losses adversely affect the superresolution process, because they lower both the transmission resonance of the evanescent modes and the transmission of the propagative modes. It is important to point out that an analysis of the influence of the losses on the superresolution capabilities of a NIM has also been studied in [20], where a logarithmic dependence of the minimum resolved distance has been analytically calculated in the limit of low losses [ $\text{Im}(\hat{n}) \ll 1$ ]. Our analysis differs from that one for two fundamental aspects. First, we analyze also the cases of high losses and, second, we assess our results based on a power analysis (time-averaged Poynting vector) rather than on the electric or magnetic field separately. At this point, we would like to point out, using the words of Born and Wolf [21], that "in optics the (averaged) Poynting vector is the chief quantity of interest." As we have already

mentioned in Section 1, currently available metamaterials are still characterized by high losses and low FOMs [11–15], and therefore a sound theoretical analysis of the limit of high losses, based on the Poynting vector, seems in order. In fact, as it will become clear later, our analysis shows that absorption does not always play a detrimental role for superresolution purposes.

In Fig. 5 we show the diffraction figures and the minimum resolved distance when the  $z$  component of the Poynting vector ( $S_z$ ) is used for a FOM respectively of  $\sim 3500$  [Fig. 5(a)],  $\sim 350$  [Fig. 5(b)],  $\sim 35$  [Fig. 5(c)], and  $\sim 3.5$  [Fig. 5(d)]. The fact that  $S_z$  is negative on the lateral parts of the diffraction figures is due to the interference of propagating and evanescent modes that can cause circulation in the Poynting vector, as previously noted [22]. In Fig. 6 we show the scaling law for  $D_{\min}$ :

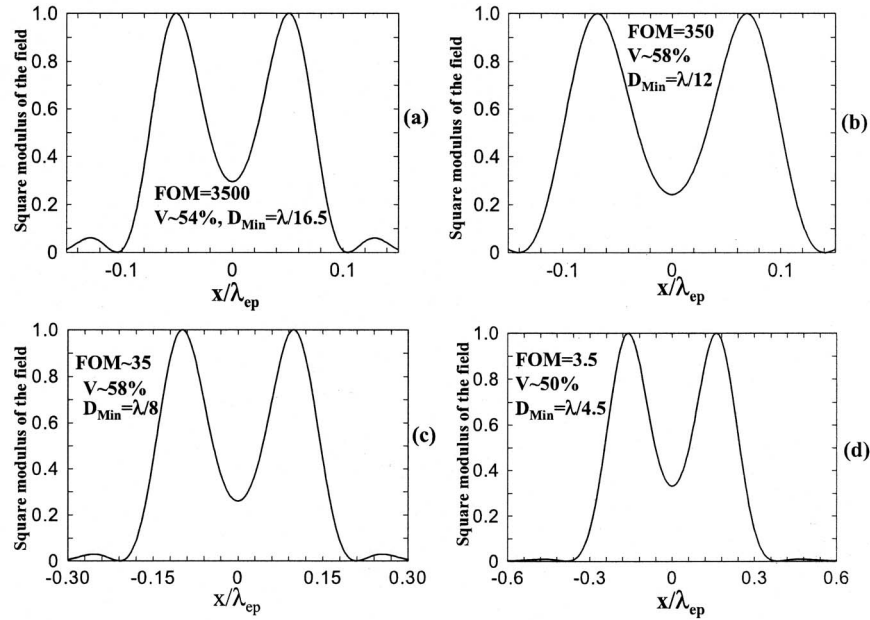


Fig. 3. Diffraction figures from the two pointlike sources on the image plane, respectively, for a (a) FOM  $\sim 3500$  and  $D_{Min} = \lambda/16.5$ , (b) FOM  $\sim 350$  and  $D_{Min} = \lambda/12$ , (c) FOM  $\sim 35$  and  $D_{Min} = \lambda/8$ , and (d) FOM  $\sim 3.5$  and  $D_{Min} = \lambda/4.5$ . The image contrast ( $V$ ) is approximately 50% in all cases. The square modulus of the field is referred to the electric field for TE polarization or to the magnetic field for TM polarization.  $D_{Min}$  is the minimum resolved distance that corresponds to a visibility  $V \sim 50\%$ . In all the figures the maximum value of the field at the image plane has been normalized to 1.

$$D_{Min} \cong \begin{cases} \frac{\lambda}{1.8 \log(\text{FOM})} \cong \frac{\lambda}{1.8 |\log(\text{Im}(\hat{n}))|} & \text{for } \text{FOM} \gg 1, \text{Im}(\hat{n}) \ll 1 \\ 0.4\lambda & \text{for } 0 \leq \text{FOM} \leq 1, \text{Im}(\hat{n}) \cong 1 \end{cases} \quad (2)$$

For  $\text{FOM} \ll 1$ ,  $D_{min}$  still scales as  $0.4\lambda$ ; for high values of the FOM, the scaling law is slightly different with respect to the previous case ( $\sim 10\%$  less in resolving power).

Although in this case the field analysis and the Poynting vector analysis give results qualitatively similar, it

should be underlined that this is not always the case, and one should always resort to the Poynting vector in order to assess the superresolution performances of a metamaterial. We will provide an example later in which the field analysis and the Poynting vector analysis give different

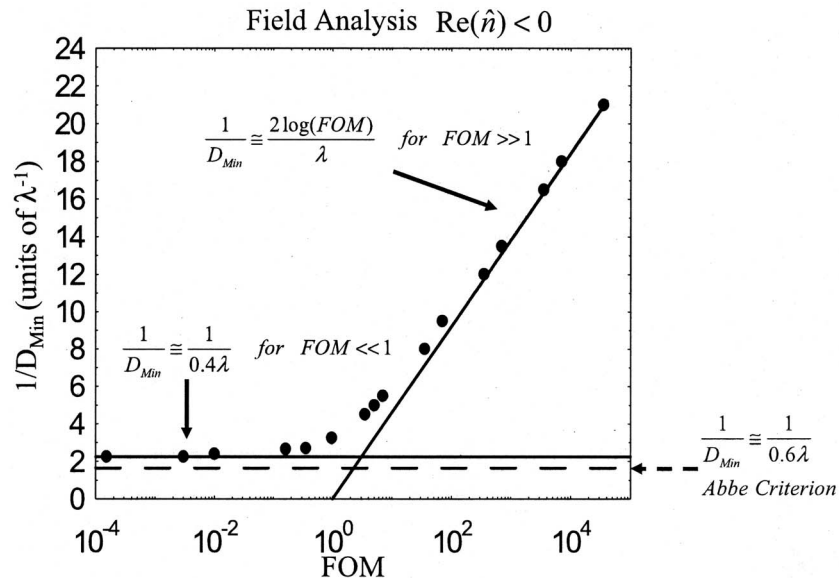


Fig. 4.  $1/D_{Min}$  (solid circles) versus FOM according to a field analysis. For  $\text{FOM} \gg 1$  the minimum resolved distance ( $D_{Min}$ ) scales as  $\lambda/(2 \log(\text{FOM}))$ , while for  $\text{FOM} \ll 1$  the minimum resolved distance scales as  $0.4\lambda$ . The dashed horizontal line represents the limit imposed by the Abbe criterion.



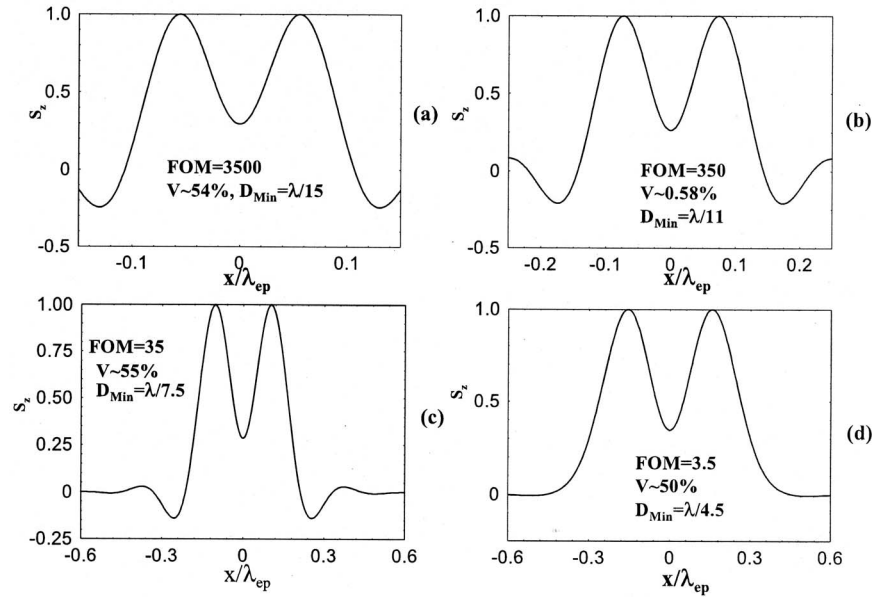


Fig. 5. Diffraction figures calculated through the Poynting vector for (a) a FOM $\sim$ 3500 and  $D_{Min}=\lambda/15$ , (b) FOM $\sim$ 350 and  $D_{Min}=\lambda/11$ , (c) FOM $\sim$ 35 and  $D_{Min}=\lambda/7.5$ , and (d) FOM $\sim$ 3.5 and  $D_{Min}=\lambda/4.5$ . In all the figures the maximum of the  $z$  component of the Poynting vector ( $S_z$ ) has been normalized to 1.

results. For the time being let us comment on Fig. 6. For  $0 \leq \text{FOM} \leq 1$  there is a characteristic plateau at  $0.4\lambda$  in the superresolution capability of the lens, which still represents a remarkable improvement of  $\sim 30\%$  over the limit of  $0.6\lambda$  imposed by the Abbe criterion. The plateau is reached for values of the damping coefficient  $\tilde{\gamma}$  close to  $1/\sqrt{2}$ . It is interesting that even in the extreme case of  $\tilde{\gamma} = 1/\sqrt{2}$  where FOM=0 and  $\hat{\epsilon}=\hat{\mu}=\hat{n}=i$  (i.e., the metamaterial becomes an impedance-matched material having a zero real part of the refractive index), the lens still resolves at  $0.4\lambda$ , i.e., beating the Abbe criterion. In this sense the FOM is not always a good indicator of the superresolution capabilities of an NIM. In Fig. 7(a) we show

the transmittance  $|t|^2$  of the slab as function of the transverse wave vector ( $k_x$ ) normalized to the vacuum wave vector ( $k_0$ ) for the case  $\tilde{\gamma}=1/\sqrt{2}$ , and in Fig. 7(b) we show a 3-D topographic plot of the transmittance versus  $k_x/k_0$  and  $\tilde{\gamma}$ . Regarding Fig. 7(a), the transmission resonance at  $k_x/k_0 > 1$ , which is the transmission resonance for the evanescent modes, indicates that the evanescent modes are somewhat “amplified” and they contribute to the image formation with subwavelength details. Of course, amplification of the evanescent modes is just one of the two key elements to obtain superresolution; the second key element is the suppression of the diffraction of the propagation modes. In this case, different from the case

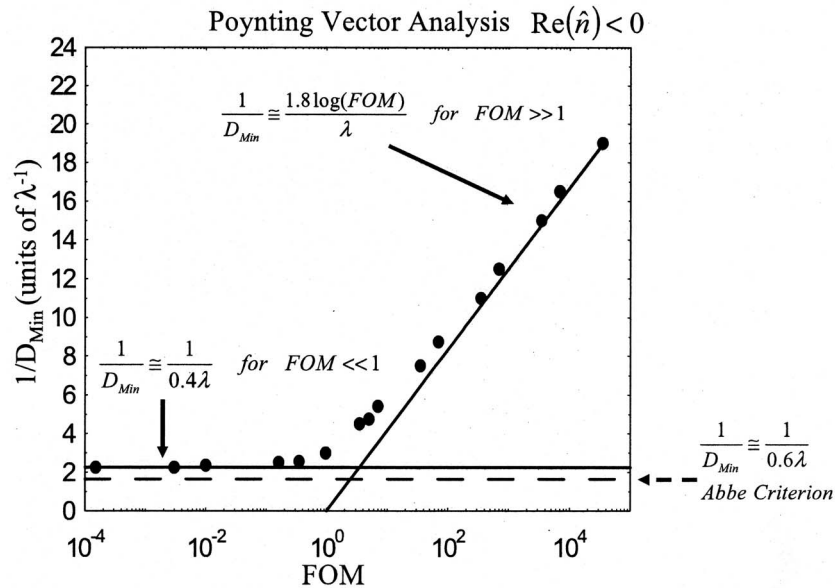


Fig. 6.  $1/D_{Min}$  (solid circles) versus FOM when the Poynting vector is considered. For FOM $\gg$ 1 the minimum resolved distance ( $D_{Min}$ ) scales as  $\lambda/[1.8 \log(\text{FOM})]$ , while for FOM $\ll$ 1 the minimum resolved distance scales as  $0.4\lambda$ . The dashed horizontal line represents the limit imposed by the Abbe criterion.

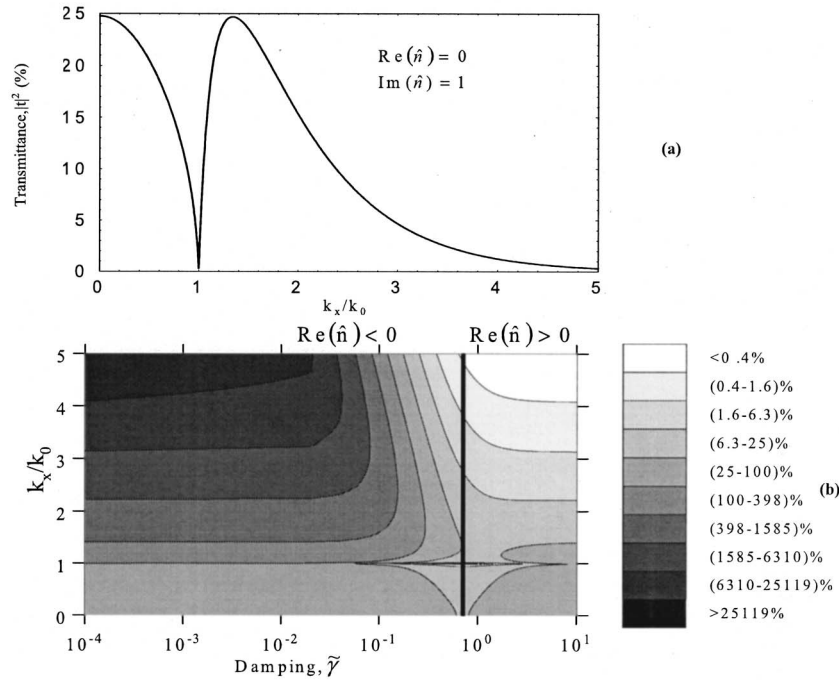


Fig. 7. (a) Transmittance  $|t|^2$  of the NIM versus  $k_x/k_0$  for  $\tilde{\gamma}=1/\sqrt{2}$ . (b) 3-D topographic plot of the transmittance versus  $k_x/k_0$  and  $\tilde{\gamma}$ . The vertical solid line indicates the position of  $\tilde{\gamma}=1/\sqrt{2}$ , where  $\text{Re}(\hat{n})=0$ .

$\hat{\epsilon}=\hat{\mu}=\hat{n}=-1$ , the rays no longer form a focus inside the lens but go parallel as in a perfect collimator, as shown in Fig. 8 and, although the suppression of the diffraction is achieved only in the lens, this is sufficient to obtain image formation. Figures 8(a) and 8(b) exemplify the two limit regimes, i.e., the regime of ideal focusing and the regime of collimation. Of course, by increasing the value of the damping term the lens passes gradually from the ideal focusing to a regime of less-than-ideal focusing with aberrations coming into play and then finally approaches the

regime of collimation. The reader can easily convince himself that an impedance-matched metamaterial having  $\text{Re}(\hat{n})=0$  acts as a perfect collimator by a simple plane-wave analysis. The refraction angle of the Poynting vector ( $\vartheta_{\vec{S}}$ ) for a plane, monochromatic wave incident on our impedance-matched metamaterial (i.e.,  $\hat{\epsilon}=\hat{\mu}=\hat{n}$ ) from vacuum at an angle  $\vartheta_0$  with respect to the normal at the interface is given by the following formula:

$$\tan(\vartheta_{\vec{S}}) = \frac{\text{Re}(\hat{n}) \sin \vartheta_0}{([\text{Re}(\hat{n})]^2 + [\text{Im}(\hat{n})]^2) \text{Re} \left( \sqrt{1 - \frac{\sin^2 \vartheta_0}{\hat{n}^2}} \right)}. \quad (3)$$

From Eq. (3) it follows that  $\vartheta_{\vec{S}}=0$  for any incident angle  $\vartheta_0$  whenever  $\text{Re}(\hat{n})=0$ . It must be noted that some properties of impedance-matched metamaterials having a zero index of refraction have also been studied in [23]. In particular, in [23] the property of those materials to convert wavefronts with small curvature into output beams with large curvature (planar) wavefronts was numerically investigated through finite-difference time-domain simulations. A single slab of silver at the wavelength of 324 nm has practically a purely imaginary permittivity  $\hat{\epsilon} \cong 0.74i$  [24], and therefore it will behave for TM light polarization similarly to the case of the NIM with a FOM=0 that we have just described. We have in fact calculated the super-resolution of a layer of Ag at the operative wavelength of  $\lambda=324$  nm for the same geometry described in Fig. 1 and find that the minimum resolved distance is approximately  $0.4\lambda$ , i.e., the same as for the case described above.

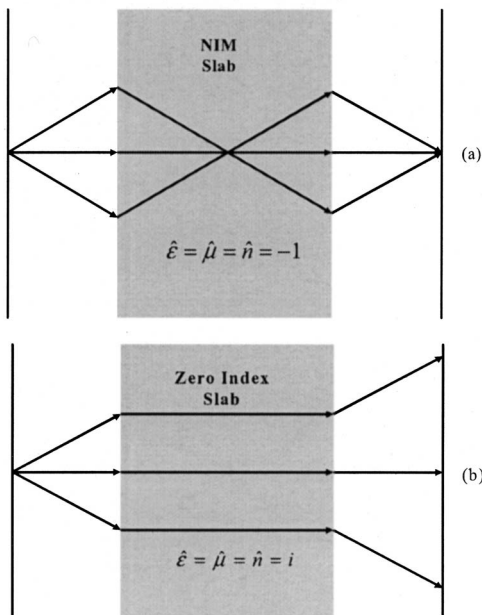


Fig. 8. Schematic picture of the rays inside a slab with (a)  $\hat{\epsilon}=\hat{\mu}=\hat{n}=-1$  and (b)  $\hat{\epsilon}=\hat{\mu}=\hat{n}=i$ .

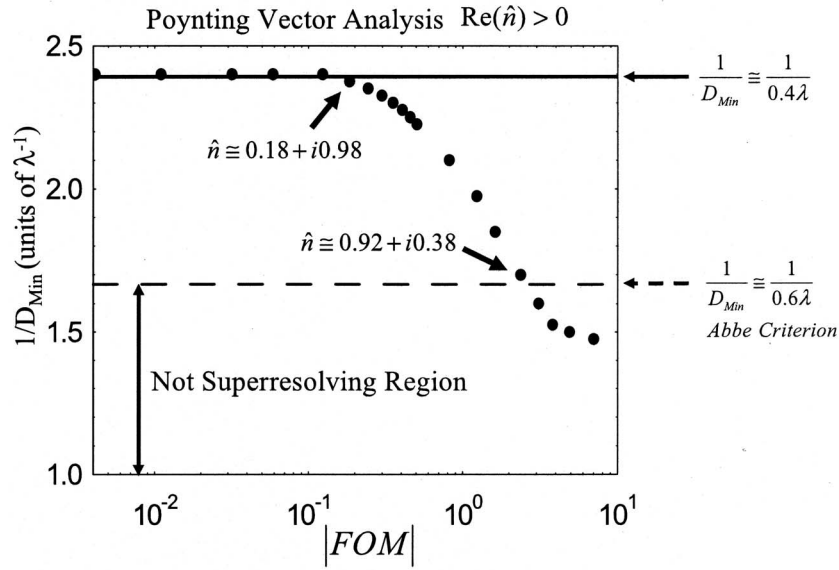


Fig. 9.  $1/D_{\text{Min}}$  (solid circles) versus  $|FOM|$  for  $FOM < 0$ . The dashed horizontal line represents the limit imposed by the Abbe criterion. Also indicated in the figure is the refractive index of the metamaterial at some particular points.

### 3. SUPERRESOLUTION FOR $\tilde{\gamma} > 1/\sqrt{2}$ ( $FOM < 0$ )

In this case the metamaterial starts to behave as a PIM with  $\text{Re}(\hat{\epsilon}) = \text{Re}(\hat{\mu}) = \text{Re}(\hat{n}) > 0$  and  $FOM < 0$ ; moreover, the imaginary part of the refractive index starts to decrease (see Fig. 2). We have varied the damping parameter  $\tilde{\gamma}$  in the range  $[1/\sqrt{2}, 10]$  that corresponds to varying the FOM approximately in the range  $[0, -7]$  and varying  $\text{Re}(\hat{\epsilon}) = \text{Re}(\hat{\mu}) = \text{Re}(\hat{n})$  approximately in the range  $[0, 1]$  (see Fig. 2). In Fig. 9 we show  $1/D_{\text{min}}$  versus the absolute value of the FOM. Quite surprisingly the figure shows that the metamaterial superresolves until the FOM reaches the value of approximately  $-2.37$ , which gives the minimum resolved distance at  $\sim 0.6\lambda$ , which is the limit of the Abbe criterion. For a  $FOM = -2.37$  the material parameters are respectively  $\tilde{\gamma} \approx 3.5$  and  $\hat{\epsilon} = \hat{\mu} = \hat{n} \approx 0.92 + i0.38$ . This is an interesting result, because it tells us that even a metamaterial with the real part of the permittivity and permeability close to 1 can superresolve in principle. The implications for the practical design of a metamaterial are important; in fact, this basically means that negative values of either the permittivity or the permeability (or both of them) are not necessary for superresolution purposes. For  $\tilde{\gamma} > 3.5$  the transmittance of the evanescent modes is even greater than that for  $\tilde{\gamma} \approx 1/\sqrt{2}$  (see Fig. 7). In fact, for  $\tilde{\gamma} > 3.5$  the superresolution is lost because of the loss of the canalization regime [25]; in other words, the metamaterial no longer superresolves, because it can no longer compensate for the diffraction of the propagative modes. From Eq. (3) we can infer that the refracted rays go parallel inside the metamaterial for any incident angle, as described in Fig. 8(b), whenever one of the following conditions is met: (a)  $|\text{Re}(\hat{n})| \ll \text{Im}(\hat{n})$ , (b)  $|\text{Re}(\hat{n})| \gg \text{Im}(\hat{n})$  and  $|\text{Re}(\hat{n})| \gg 1$ . The condition  $\tilde{\gamma} = 1/\sqrt{2}$  represents the case of perfect collimation, because the real part of the refractive index is exactly zero. Increasing the value of the damping over  $1/\sqrt{2}$  causes the real part of the refractive index to

increase and its imaginary part to decrease (see Fig. 2); therefore the effect of the collimation will be gradually lost. In this sense, in the case at hand, the decreasing of the absorption plays two antithetical roles: On one hand it improves the transmission of the evanescent modes, but on the other hand it causes the loss of collimation of the propagative modes. The superresolution is lost when the beneficial effect of the better transmission of the evanescent modes is no longer able to compensate the detrimental effect of the loss of collimation. If anything, what our discussion shows is that the imaginary part of the refractive index does not always play a detrimental role, but in some circumstances its role can even be beneficial regarding superresolution. This finding may be of some help in the practical design of metamaterials. Given the fact that consistent losses in currently available metamaterials seem unavoidable, one may take advantage of those losses that exploit those particular regimes. As a final example, in Section 4 we would like to analyze the realistic case of a single layer of silver.

### 4. SINGLE LAYER OF SILVER

First of all, let us study the spectral region where surface plasmon polariton modes (SPPs) exist for an air–silver interface. The complex dispersion of the SPPs at the air–silver interface is given by [26]

$$\hat{k}_{\text{SPP}} = k_0 \left( \sqrt{\frac{\hat{\epsilon}}{1 + \hat{\epsilon}}} \right), \quad (4)$$

where  $\hat{\epsilon}$  is the complex permittivity of silver and  $k_0$  is the vacuum wavevector. SPPs are in general guided modes that may exist at the interface of dielectric–metal; these modes are also nonradiative in nature, i.e.,  $\text{Re}(\hat{k}_{\text{SPP}}) > k_0$  in the case air–metal. In Fig. 10 we show the effective index defined as  $\hat{n}_{\text{SPP}} = \hat{k}_{\text{SPP}}/k_0$ . The spectral region where SPPs are found is defined by the condition  $\text{Re}(\hat{n}_{\text{SPP}}) > 1$ .



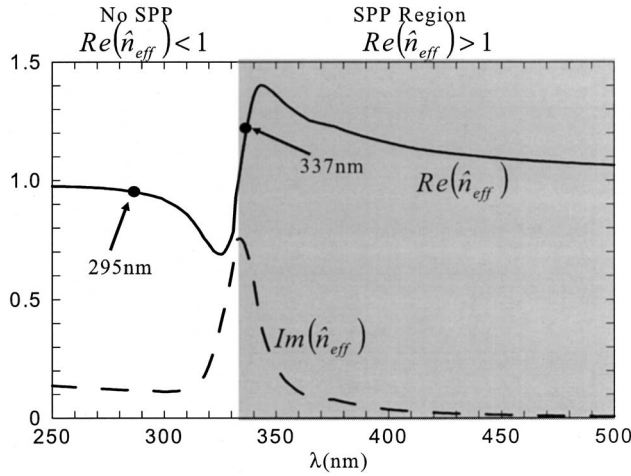


Fig. 10. Effective index  $\text{Re}(\hat{n}_{\text{eff}})$  and extinction coefficient  $\text{Im}(\hat{n}_{\text{eff}})$  versus wavelength for SPPs at the air–silver interface. The shaded area indicates the region where SPPs exist. In the figure are also indicated the wavelength of 337 nm, where  $\text{Re}(\epsilon_{\text{Ag}}) \approx -1$ , and the wavelength of 295 nm, where  $\text{Re}(\epsilon_{\text{Ag}}) \approx 1.13$ .

The values of the permittivity of silver are taken from experimental data [24]. Conventional wisdom would say that a silver layer superresolves only in a certain region around 337 nm, where  $\text{Re}(\hat{\epsilon}) \approx -1$  and where SPPs can be excited. The condition  $\text{Re}(\hat{\epsilon}) \approx -1$  assures the compensation of the diffraction through the focusing mechanism described in Fig. 8(a), while the excitation of a SPP, given its nonradiative nature, ensures that the structure supports evanescent modes. We now show that a single layer of silver can superresolve for TM light polarization with a minimum resolved distance of  $\sim \lambda/3$  ( $\sim 50\%$  better than the limit of  $0.6\lambda$  imposed by the Abbe criterion) for an operative wavelength of  $\lambda = 295$  nm, i.e., well beyond its plasma frequency [ $\lambda_{\text{ep,Ag}} = 328$  nm (3.78 eV)], where SPPs cannot be excited and the real part of the permittivity is positive. The geometry is described in Fig. 11(a). In this case, different from the geometry of Fig. 1, the two slits are located at the entrance of the lens (but in free space), and the image is placed at the end face of the lens. In this way we have the canalization mechanism taking place inside the lens, and at the same time, by having the image and the object plane attached respectively at the output and input surface of the lens, we avoid diffraction outside the lens. The distance of the object plane from the image plane is the same fraction of the operative wavelength as in Fig. 1. The refractive index of silver at 295 nm is  $\hat{n} \approx 1.52 + i1.08$  [24], and the permittivity is  $\hat{\epsilon} \approx 1.13 + i3.3$ . In Fig. 11(b) we show that the two point sources located in the object plane with a mutual distance of  $D = \lambda/3$  are resolved in the image plane with a visibility  $V \sim 52\%$ , which unambiguously proves superresolution. It should be therefore clear that the excitation of plasmonic modes is not necessary for superresolution purposes. Without the Ag layer in place the visibility would be  $V \sim 5\%$  (i.e., 1 order of magnitude less). The minimum resolved distance without the Ag layer is  $D_{\text{min}} \sim 0.8\lambda$ . Again, superresolution for TM polarization is possible because a) there is a resonance in the transmittance of the evanescent modes and b) the propagative modes are canalized inside the

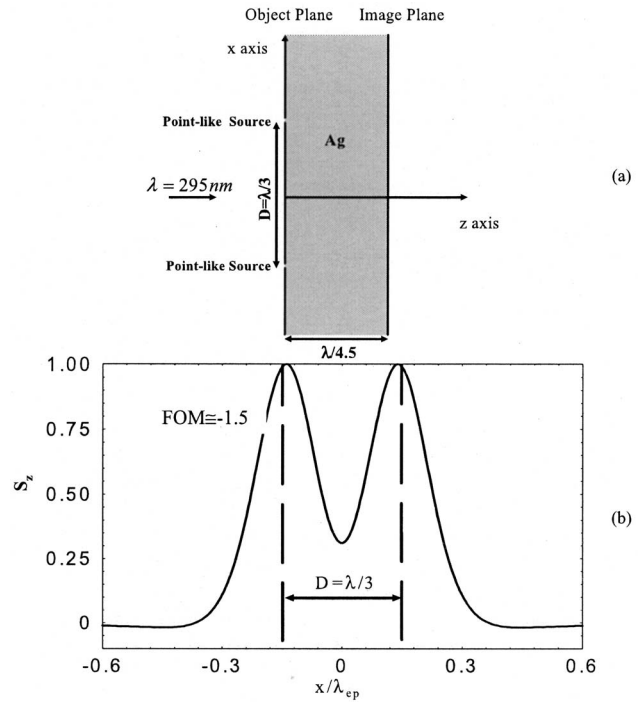


Fig. 11. (a) Geometry used for superresolution from a single layer of silver at  $\lambda = 295$  nm. (b) Image of the two pointlike sources for TM polarization. The visibility is approximately 52%. The vertical dashed lines indicate the position of the pointlike sources in the object plane.  $S_z$  is normalized to 1.

layer. Let us first analyze the canalization process in this case. A simple analysis can show that the refraction angle of the Poynting vector ( $\vartheta_{\vec{S}}$ ) for a plane, monochromatic wave incident on generic material from vacuum at an angle  $\vartheta_0$  with respect to the normal at the interface is given by the following formulas:

$$\tan(\vartheta_{\vec{S}}) = \frac{\text{Re}(\hat{\epsilon}) \sin \vartheta_0}{|\hat{\epsilon}|^2 \text{Re}\left(\frac{\hat{n}}{\hat{\epsilon}} \sqrt{1 - \frac{\sin^2 \vartheta_0}{\hat{n}^2}}\right)} \quad (\text{TM polarization}), \quad (5a)$$

$$\tan(\vartheta_{\vec{S}}) = \frac{\text{Re}(\hat{\mu}) \sin \vartheta_0}{|\hat{\mu}|^2 \text{Re}\left(\frac{\hat{n}}{\hat{\mu}} \sqrt{1 - \frac{\sin^2 \vartheta_0}{\hat{n}^2}}\right)} \quad (\text{TE polarization}). \quad (5b)$$

In Fig. 12 we show the refracted angle of the Poynting vector as a function of the incident angle for the case of Ag at 295 nm. It is evident that the canalization process is taking place only for TM polarization of the light, although not in an ideal way. In Fig. 13 we show the transmittance versus  $k_x/k_0$ . In this case the transmission of the evanescent modes is effective just for TM polarization. The fact that a material with a real part of the refractive index greater than 1 may support evanescent modes should not be surprising. Amplification of evanescent waves by two dielectric planar waveguides was, for example, analytically demonstrated in [27]. The conditions and the geometry studied in [27] are different from ours;

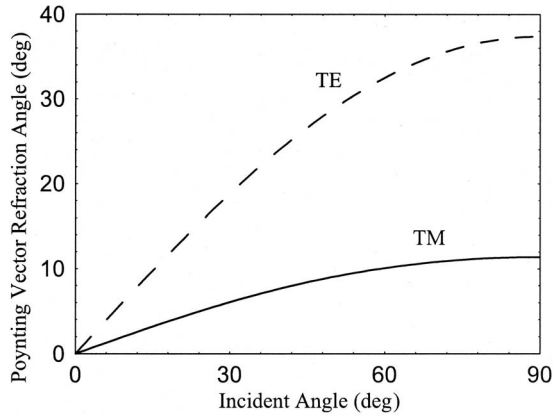


Fig. 12. Refraction angle of the Poynting vector versus the incident angle at the air–silver interface for a wavelength of 295 nm. The dashed curve is for TE polarization, and the solid curve is for TM polarization.

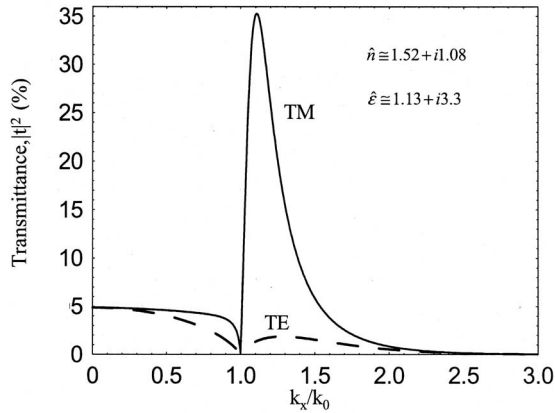


Fig. 13. Transmittance  $|t|^2$  of the silver layer at 295 nm vs  $k_x/k_0$ .

nevertheless, the physical reasons underlying the supporting of evanescent waves are essentially the same, i.e., in our case the single layer of Ag at 295 nm acts as if it were a dielectric waveguide with strong losses, and therefore it is able to couple part of the evanescent modes that become quasi-guided modes inside the layer. To be as clear as possible regarding the physical origin of the amplification of the evanescent modes in a slab with  $n > 1$ , we would like to remark that any time guided modes are excited in the transverse direction ( $x$  axis)—being either plasmonic modes or just conventional guided modes—the transmittance  $T(k_x)$  along the  $z$  axis will show resonances (amplification) in the evanescent part of the spectrum exactly at the  $k_x$  terms where those guided modes are excited. In this sense there is a unifying concept that lies behind the amplification of the evanescent modes in a single layer of metal with  $\text{Re}(\hat{\epsilon}) = -1$  for TM polarization and in a simple slab of dielectric material with  $\text{Re}(\hat{n}) > 1$ . In both cases amplification of the evanescent modes happens when guided modes are excited in the transverse direction; in the first case they are SPP mode, whereas in the latter case they are conventional guided modes. Of course, in the example we have proposed, the price to pay in order to obtain a good degree of superresolution ( $D_{\min} = \lambda/3$ ) in a region where plasmonic modes are not involved is that the transparency of the lens is not high; only  $\sim 5\%$  of the

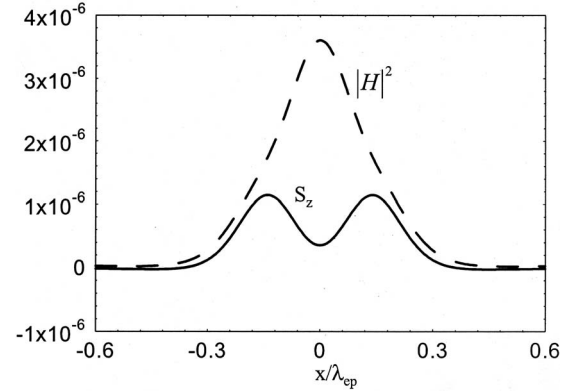


Fig. 14. Comparison between  $S_z$  and  $|H|^2$  for the geometry described in Fig. 11. We have used nondimensional units; i.e., we take  $\epsilon_0 = \mu_0 = c = 1$  and unitary amplitude for the electric and magnetic field of the plane, monochromatic, TM-polarized wave incident on the screen. In those nondimensional units the intensity carried by the plane wave is  $S_{z,pw} = 0.5$ .

incident power is transmitted to the other side. We have also calculated the superresolution with the Ag layer for the same geometry described in Fig. 1, i.e., for a distance of  $\lambda/18$  between the object (image) plane and the beginning (end) of the lens and a thickness of the Ag layer of  $\lambda/9$ . Although the TM transmittance for both propagative and evanescent modes greatly improves with respect to the previous case because half of the thickness of Ag is now used, the visibility of the image drops to  $V \sim 15\%$ , because the canalization process is now less effective owing to the fact that it is taking place in just half of the distance between the image plane and the object plane. Finally, we would like to come back to the issue of the field analysis versus Poynting vector analysis. In Fig. 14 we show the square modulus of magnetic field ( $|H|^2$ ) and  $S_z$  for the case of Fig. 11. It is clear that the two quantities differ significantly from each other in shape. A field analysis in this case would be inappropriate in order to assess the superresolution performances of the object.

## 5. CONCLUSIONS

We have discussed the influence of the losses of an impedance-matched NIM on its superresolving capability. The NIM has been described by a lossy Drude model with equal permittivity and permeability. The analysis has been performed using the Poynting vector as the chief quantity of interest instead of the electric or magnetic fields separately. We have found that in the limit of low losses [ $\text{Im}(\hat{n}) \ll 1$ ] the minimum resolved distance  $D_{\min}$  scales as  $D_{\min} \approx \lambda / [1.8 |\log(\text{Im}(\hat{n}))|]$ , while in the limit of high losses [ $\text{Im}(\hat{n}) \sim 1$ ]  $D_{\min} \approx 0.4\lambda$ . By varying the damping parameter in the Drude model we have also explored the case where both the permittivity and permeability are positive, and we have found that the metamaterial still continues to superresolve until the real part of the refractive index becomes close to 1. We have discussed the physical mechanisms behind the superresolution when the permittivity and permeability are both positive. We have also provided an example of superresolution at  $\sim \lambda/3$  from a single layer of Ag well beyond its plasma frequency, where plasmonic modes are not excited and the

real part of the permittivity is  $\sim 1$ . It is also worthwhile noting that in all the cases we have determined that the superresolution is lost very rapidly once the image plane is placed one or two wavelengths away from the end of the lens.

We hope that our results may be of some guidance for the future design of metamaterials for superresolution purposes.

## APPENDIX A

In this Appendix we give full details on the calculation method used. We consider nondimensional units, i.e., we take  $\varepsilon_0 = \mu_0 = c = 1$  ( $\varepsilon_0$  and  $\mu_0$  are respectively the permittivity and permeability of vacuum, and  $c$  is the speed of light in vacuum). Let us start by discussing the calculation method for TM polarization of the incident light. The calculations of the diffraction figures on the image plane have been carried out using the technique of the angular spectrum decomposition [28] in conjunction with the transfer-matrix technique [29]. Referring to Fig. 1, a plane, monochromatic, TM-polarized wave of unitary amplitude and with wave vector  $k_0 = 2\pi/\lambda$  is incident on the object plane that is at a distance  $d_1$  from the input surface of the NIM slab of length  $L$ . The input surface of the NIM slab is located at  $z=0$  along the  $z$  axis, the object plane is

located at  $z=-d_1$ , and the image plane is located at  $z=L+d_2$ . In our reference frame, the magnetic field diffracted from the object plane is expressed as

$$\vec{H}(x, z, t) = (1/2)[\vec{H}(x, z)\exp(-i\omega t) + \text{c.c.}], \quad (\text{A1})$$

where  $\vec{H}(x, z) = H(x, z)\hat{y}$  is the complex, stationary vector field,  $\hat{y}$  is the unit vector of the  $y$  axis, c.c. stands for complex conjugate, and the reference system  $(x, y, z)$  forms a right-hand term. The complex amplitude of the magnetic field  $H(x, z)$  diffracted in the semispace beginning at the output of the lens, i.e., at  $z \geq L$ , is expressed by the following integral [28]:

$$H(x, z \geq L) = \int_{-\infty}^{+\infty} A(k_x) t_{TM}(k_x) \times \exp[i(k_x x + \sqrt{k_0^2 - k_x^2}(d_1 + z - L))] dk_x. \quad (\text{A2})$$

Here  $k_x$  is a real quantity and represents physically the wave vector of the  $x$  axis;  $t_{TM}(k_x)$  is the complex transmission function of the NIM slab for TM polarization, transmission function that has been calculated using a transfer-matrix technique [29]. Because we are dealing with a single slab placed in vacuum, the transmission function can be explicitly expressed in following form:

$$t_{TM}(k_x) = \frac{2}{2 \cos\left(\hat{n} \sqrt{k_0^2 - \frac{k_x^2}{\hat{n}^2}} L\right) - i \left( \frac{\hat{n} \sqrt{k_0^2 - \frac{k_x^2}{\hat{n}^2}}}{\hat{\varepsilon} \sqrt{k_0^2 - k_x^2}} + \frac{\hat{\varepsilon} \sqrt{k_0^2 - k_x^2}}{\hat{n} \sqrt{k_0^2 - \frac{k_x^2}{\hat{n}^2}}} \right) \sin\left(\hat{n} \sqrt{k_0^2 - \frac{k_x^2}{\hat{n}^2}} L\right)}. \quad (\text{A3})$$

The magnetic field at the image plane can be calculated from Eq. (A2) by putting  $z = L + d_2$ . Note that the integral [Eq. (A2)] extends over both the propagative ( $|k_x| \leq k_0$ ) and evanescent modes ( $|k_x| > k_0$ ).  $A(k_x)$  is the Fourier spectrum of the magnetic field on the object plane. In particular, in our case,  $A(k_x)$  is nothing else than the Fourier transform (FT) of the transmission function of the screen located at  $z = -d_1$ :

$$A(k_x) = \text{FT}(t_{\text{screen}}(z = -d_1, x)), \quad (\text{A4})$$

where the transmission function of the screen is defined as

$$t_{\text{screen}}(z = -d_1, x) = \begin{cases} 0 & -\infty < x < -D/2 - a_1 \\ 1 & -D/2 - a_1 \leq x \leq -D/2 \\ 0 & -D/2 < x < D/2 \\ 1 & D/2 \leq x \leq D/2 + a_2 \\ 0 & D/2 + a_2 < x < \infty \end{cases}. \quad (\text{A5})$$

In practice, the transmission of the screen describes two slits respectively of width  $a_1$  and  $a_2$  located at a mutual

distance (center to center) of  $D + (a_1 + a_2)/2$ . Basically Eq. (A5) is the sum of two rectangular (rect) functions. The FT of Eq. (A5) can, of course, be performed analytically in terms of a linear superposition of sine cardinal (sinc) functions. In our case we have taken the width of the two slits so that  $a_1 = a_2 = \lambda/500$ , where  $\lambda$  is the wavelength of the incident radiation; in this way, for all intents and purposes, the two slits can be considered as pointlike sources. Once the complex amplitude of the magnetic field is calculated by means of the integral expressed in Eq. (A2), we can calculate the complex amplitude of the electric field by applying the “curl” operator to the magnetic field as follows:

$$\nabla \times \vec{H} = -i\omega \vec{E}. \quad (\text{A6})$$

Equation (A6) is the differential form of the generalized Ampere law in vacuum for time-harmonic fields in their complex representation [18]. Once the complex amplitude of the electric field is calculated, the Poynting vector can be calculated by the well-known formula [29]

$$\tilde{S} = (1/2)\text{Re}[\tilde{E} \times \tilde{H}^*]. \quad (\text{A7})$$

The calculations for a TE-polarized wave follow the same procedure outlined above, except that the integral [Eq. (A2)] is calculated for the electric field, the transmission of the NIM slab is for TE polarization, and the calculation of the magnetic field from the electric field is done by using the differential form of Faraday's law of induction. Note also that the transmission for TE polarization can be obtained using Eq. (A3) with the formal substitution  $\varepsilon \rightarrow \mu$ . In the particular case of an impedance-matched medium, i.e.,  $\hat{\varepsilon} = \hat{\mu} = \hat{n}$ , the transmission function  $t(k_x)$  for TE and for TM polarization is the same.

We would like to underline that the angular-spectrum representation applied to layered structures is a semianalytical technique that relies on the calculation of a simple one-dimensional scattering integral containing well-behaved functions. In problems of diffraction in the near field (especially when plasmon modes are involved), this technique avoids spurious effects that might arise using full numerical simulations, as pointed out in [30,31].

## ACKNOWLEDGMENT

G. D'Aguanno and N. Mattiucci thank the National Research Council for financial support.

## REFERENCES AND NOTES

1. V. G. Veselago, "The electrodynamics of substances with simultaneously negative values of  $\varepsilon$  and  $\mu$ ," *Sov. Phys. Usp.* **10**, 509–514 (1968).
2. J. B. Pendry, "Negative refraction makes a perfect lens," *Phys. Rev. Lett.* **85**, 3966–3969 (2000) and references therein.
3. R. A. Shelby, D. R. Smith, and S. Schultz, "Experimental verification of a negative index of refraction," *Science* **292**, 77–79 (2001).
4. C. G. Parazzoli, R. B. Greengard, K. Li, K. E. C. Koltenbah, and M. Tanielian, "Experimental verification and simulation of negative index of refraction using Snell's law," *Phys. Rev. Lett.* **90**, 107401-1-4 (2003).
5. S. Linden, C. Enkrich, M. Wegener, J. Zhou, T. Koschny, and C. M. Soukoulis, "Magnetic response of metamaterials at 100 terahertz," *Science* **306**, 1351–1353 (2004).
6. G. D'Aguanno, N. Mattiucci, M. Scalora, and M. J. Bloemer, "Bright and dark gap solitons in a negative index Fabry–Perot etalon," *Phys. Rev. Lett.* **93**, 213902-1-4 (2004).
7. G. D'Aguanno, N. Mattiucci, M. Scalora, and M. J. Bloemer, "TE and TM guided modes in an air waveguide with a negative-index-material cladding," *Phys. Rev. E* **71**, 046603-1-7 (2005).
8. G. D'Aguanno, N. Akozbek, N. Mattiucci, M. Scalora, M. J. Bloemer, and A. M. Zheltikov, "Dispersion-free pulse propagation in a negative-index material," *Opt. Lett.* **30**, 1998–2000 (2005).
9. M. Bloemer, G. D'Aguanno, M. Scalora, and N. Mattiucci, "Broadband omnidirectional reflection from negative index materials," *Appl. Phys. Lett.* **87**, 261921-1-3 (2005).
10. S. Zhang, W. Fan, N. C. Panoiu, K. J. Malloy, R. M. Osgood, and S. R. J. Brueck, "Experimental demonstration of near-infrared negative-index metamaterials," *Phys. Rev. Lett.* **95**, 137404-1-4 (2005).
11. V. M. Shalaev, W. Cai, U. K. Chettiar, H. Yuan, A. K. Sarychev, V. P. Drachev, and A. V. Kildishev, "Negative index of refraction in optical metamaterials," *Opt. Lett.* **30**, 3356–3358 (2005).
12. S. Zhang, W. Fan, K. J. Malloy, S. R. J. Brueck, N. C. Panoiu, and R. M. Osgood, "Near-infrared double negative metamaterials," *Opt. Express* **13**, 4922–4930 (2005).
13. G. Dolling, C. Enkrich, M. Wegener, C. M. Soukoulis, and S. Linden, "Low-loss negative-index metamaterial at telecommunication wavelengths," *Opt. Lett.* **31**, 1800–1802 (2006).
14. G. Dolling, M. Wegener, C. M. Soukoulis, and S. Linden, "Negative-index metamaterial at 780 nm wavelength," *Opt. Lett.* **32**, 53–55 (2007).
15. U. K. Chettiar, A. V. Kildishev, H.-K. Yuan, W. Cai, S. Xiao, V. P. Drachev, and V. M. Shalaev, "Dual-band negative index metamaterial: double negative at 813 nm and single negative at 772 nm," *Opt. Lett.* **32**, 1671–1673 (2007).
16. M. J. Bloemer, G. D'Aguanno, N. Mattiucci, M. Scalora, and N. Akozbek, "Broadband super-resolving lens with high transparency for propagating and evanescent waves in the visible range," *Appl. Phys. Lett.* **90**, 174113-1-3 (2007).
17. K. Aydin, I. Bulu, and E. Ozbay, "Subwavelength resolution with a negative index metamaterial superlens," *Appl. Phys. Lett.* **90**, 254102-1-3 (2007).
18. M. Born and E. Wolf, *Principles of Optics*, 7th (expanded) edition (Cambridge U. Press, 1999).
19. X. Wang, Z. F. Ren, and K. Kempa, "Unrestricted superlensing in a triangular two-dimensional photonic crystal," *Opt. Express* **12**, 2919–2924 (2004).
20. R. Merlin, "Analytical solution of the almost-perfect-lens problem," *Appl. Phys. Lett.* **84**, 1290–1293 (2004) and references therein.
21. M. Born and E. Wolf, *Principles of Optics*, 7th (expanded) edition (Cambridge U. Press, 1999), page 10.
22. M.-C. Yang and K. J. Webb, "Poynting vector analysis of a superlens," *Opt. Lett.* **30**, 2382–2384 (2005).
23. R. W. Ziolkowski, "Propagation in and scattering from a matched metamaterial having a zero index of refraction," *Phys. Rev. E* **70**, 046608-1-12 (2004).
24. *Handbook of Optical Constants of Solids*, E. D. Palik, ed. (Academic, 1985).
25. The term "canalization" has been first used in P. A. Belov, C. R. Simovski, and P. Ikonen, "Canalization of subwavelength images by electromagnetic crystals," *Phys. Rev. B* **71**, 193105-1-4 (2005).
26. H. Raether, *Surface Plasmons* (Springer-Verlag, 1988).
27. M. Tsang and D. Psaltis, "Reflectionless evanescent-wave amplification by two dielectric planar waveguides," *Opt. Lett.* **31**, 2741–2743 (2006).
28. L. Mandel and E. Wolf, *Optical Coherence and Quantum Optics* (Cambridge U. Press, 1995).
29. A. Yariv and P. Yeh, *Optical Waves in Crystals* (Wiley, 1984).
30. Y. Zhao, P. Belov, and Y. Hao, "Accurate modeling of the optical properties of left-handed media using a finite-difference time-domain method," *Phys. Rev. E* **75**, 037602 (2007).
31. A. A. Sukhorukov, I. V. Shadrivov, and Yu. S. Kivshar, "Wave scattering by metamaterial wedges and interfaces," *Int. J. Numer. Model.* **19**, 105 (2006).